



Magnetic Phase Separation in Double Perovskite $\text{Sr}_2\text{TiMnO}_{5.87}$

D. V. Popov¹ · I. V. Yatsyk¹ · R. G. Batulin² · M. A. Cherosov² · I. R. Vakhitov² ·
I. A. Faizrakhmanov¹ · R. V. Yusupov² · T. I. Chupakhina³ · Yu. A. Deeva³ ·
I. I. Fazlizhanov¹ · T. Maiti⁴ · R. M. Eremina¹

Received: 3 March 2023 / Revised: 27 March 2023 / Accepted: 28 March 2023 /

Published online: 15 April 2023

© The Author(s), under exclusive licence to Springer-Verlag GmbH Austria, part of Springer Nature 2023

Abstract

The double perovskite $\text{Sr}_2\text{TiMnO}_{5.87}$ was synthesized via the solution combustion precursor method using $\text{Sr}(\text{NO}_3)_2$, MnO_2 , $i\text{-Ti}(\text{OC}_3\text{H}_7)_4$, and disubstituted ammonium citrate as a complexing agent. The crystal structure and unit cell parameters are refined by the Rietveld method using powder X-ray diffraction. The magnetic properties of double perovskites $\text{Sr}_2\text{TiMnO}_{5.87}$ were studied using the ESR spectroscopy, specific heat measurements in the temperature range $\sim 5\text{--}300$ K, and magnetometry under cooling in zero- (ZFC) and nonzero-fields (FC). The four ESR lines were observed in ESR spectra, three ESR lines with $g \sim 2$ and fourth ESR at $B_{\text{res}} = 50$ mT in both X- and Q-bands measurements in the temperature range 37.5–42 K in $\text{Sr}_2\text{TiMnO}_{5.87}$. The peaks obtained in real and imaginary parts of AC magnetization measurements confirm phase separation at the same temperatures. The antiferromagnetic ordering was found out below the temperature $T_N \approx 12$ K. The fitting Debye and Einstein temperatures, obtained from the specific heat measurements, are equal to $\theta_D = 217$ K, $\theta_{E1} = 275$ K, $\theta_{E2} = 615$ K, and $\theta_{E3} = 2000$ K.

✉ D. V. Popov
kazan-city.dvpopoff@yandex.ru

¹ Zavoisky Physical-Technical Institute, Federal Research Center “Kazan Scientific Center of RAS”, Sibirsky Tract, 10/7, 420029 Kazan, Russia

² Kazan (Volga Region) Federal University, Kremlevskaya St., 18, 420008 Kazan, Russia

³ Institute of Solid State Chemistry of the Russian Academy of Sciences (UB), Pervomaiskaya St., 91, Ekaterinburg 620990, Russia

⁴ Department of Materials Science and Engineering, Indian Institute of Technology Kanpur, Kanpur 208016, UP, India

1 Introduction

The general formula of a double perovskite is $A_2B'B''O_6$, where A is a divalent alkaline earth metal, B' and B'' are occupied by transition metals. Double perovskites remained a fascinating topic of research during the last few decades due to their unique magnetic, electrical, and dielectric properties, as well as extremely high magnetoresistance [1–3]. In addition, insulator–metal and even semimetal–metal transitions were observed in these materials [4, 5]. Exchange interactions between two 3d-ions at B'/B''-site give rise to unusual magnetic properties [6–8]. Double perovskites exhibit various ferroic behaviors, such as antiferromagnetism [9], ferromagnetism [10], magnetic frustration [11], multiferroicity [12] etc. For example, Sr_2MoFeO_6 double perovskite is a semimetal and has a ferromagnetic ordering with a Curie temperature of 415 K [2], whereas in case of Sr_2MoCoO_6 , the antiferromagnetic ordering is observed at $T_N=37$ K [1]. On the other hand, Sr_2FeTiO_6 double perovskite exhibits a non-metallic spin-glass-like state below 16 K, driven by competing interactions between the antiferromagnetic and the ferromagnetic states [13]. The magnetic ground state of the spin-1/2 square-lattice was found in antiferromagnetic $Sr_2Cu(Te_{0.5}W_{0.5})O_6$ [14]. The specific heat of $Sr_2Cu(Te_{0.5}W_{0.5})O_6$ shows a significant linear term, despite the fact that it is an insulator, and its frustration factor $f=|C_{wl}/T_N$ exceeds 3700, indicating a spin-liquid-like ground state whose nature remains unclear. In the present work, we have carried out detailed investigation on the structure and magnetic properties of double perovskite Sr_2TiMnO_6 (STM), in which the B-position is occupied by magnetic ions Mn^{4+} and non-magnetic ions Ti^{4+} . Double perovskite STM can be assumed as the combination of two simple perovskites such as incipient ferroelectric, $SrTiO_3$ and antiferromagnetic $SrMnO_3$ [15, 16].

Sr_2TiMnO_6 (STM), was studied earlier [17] for a rechargeable zinc–air battery (ZAB) with a power density of 97 mW/cm² and a specific capacity of 705.21 mAh/g. Its good cycling stability with a current density of 3.5 mA/cm² for 6.66 h makes STM a promising candidate for commercial fuel cells and metal-air batteries. The composite of STM with reduced graphene oxide composite was also reported as extremely efficient catalyst with excellent photocatalytic activity in visible light [18]. Few reports are found in the literature on the magnetic, and ferroelectric behavior of Sr_2TiMnO_6 complex perovskite produced by the solid-state reaction method [19, 20]. The authors of the papers [19, 20] found that the sample STM was crystallized in a perovskite tetragonal structure with I4/mmm space group. A paramagnetic–ferromagnetic transition was reported to occur at critical temperature of 44.8 K. The effective magnetic moment of 3.5 μ_B was obtained from the Curie constant. Below 44.8 K, it exhibits a multiferroic state [20]. Besides, two magnetic phase transitions were observed in the polycrystalline sample of Sr_2TiMnO_6 prepared by solid-state reaction at 45 K and 15 K [21]. Powder neutron diffraction studies suggest the possible antiferromagnetic ordering in this compound at 12 K with the effective magnetic moment of 0.61 μ_B at the Mn site. A large degree of disorder in the arrangement of 3d ions in position B does not allow the formation of double perovskite, and then we can only talk about the magnetic properties of perovskite.

Single-phase polycrystalline sample of perovskite $\text{SrTi}_{0.5}\text{Mn}_{0.5}\text{O}_3$ has been successfully synthesized via solid-state reaction route in [22]. The authors concluded that STMO is a disordered perovskite in which titanium and manganese ions are randomly distributed, a single anomaly in the dc magnetization and the frequency invariant maximum at ~ 13 K in ac susceptibility suggest the long-range antiferromagnetic order. On the other hand, the authors of the work [23] believe that magnetic measurements in magnetization suggest on $\text{SrMn}_{0.5}\text{Ti}_{0.5}\text{O}_3$ form spin-glass like phase at ~ 14 K. Later static and dynamic magnetic properties $\text{SrTi}_{0.5}\text{Mn}_{0.5}\text{O}_3$ prepared through a solid-state reaction route were studied in [24]. A cusp-like peak at $T_f \sim 14$ K in magnetization, which exhibits field and frequency dependence, suggests the existence of spin clusters. Also, the other features observed in magnetic memory effect, muon spin resonance/rotation and neutron powder diffraction confirm the existence of cluster of spin-glass state. That is, the nature of the phase transition is due to the degree of disorder associated with the distribution of titanium and manganese ions. If the distribution is random, then the spin-glass state is realized.

Although some reports are available on magnetic behavior of STM [25], the detailed understanding of magnetic ordering in this double perovskite is yet to be fully understood. Electron paramagnetic resonance (EPR) or electron spin resonance (ESR) measurement is a great tool to unravel the nature of magnetism in a compound. To the best of our knowledge, no reports are found in the literature on the ESR measurement of STM. In the current work, we have analyzed the magnetic data of STM synthesized by solution chemistry in correlation with ESR measurement and detailed structural and microstructural investigation with the help of XRD, XPS, SEM and EDXS.

2 Experimental Details

Polycrystalline powders of $\text{Sr}_2\text{MnTiO}_6$ perovskite were obtained via the solution combustion precursor method using $\text{Sr}(\text{NO}_3)_2$, MnO_2 , $i\text{-Ti}(\text{OC}_3\text{H}_7)_4$, and disubstituted ammonium citrate as a complexing agent. The corresponding weights of the remaining reagents were calculated by the amount of titanium isopropylate suspended in a closed box. Manganese dioxide was dissolved by heating in nitric acid in the presence of 20% disubstituted ammonium citrate. Titanium isopropylate was hydrolyzed with 70% ethyl alcohol solution, then the resulting product was dissolved in nitric acid. Strontium nitrate was dissolved in distilled water. All three solutions were mixed and the remaining ammonium citrate was added. The resulting solution was evaporated until the reaction mass ignited. The pyrolysis product was heat treated with 973 K to remove organic matter. Afterward, the sample was annealed twice at 1373 K for 8 h with intermediate grinding.

ESR measurements of $\text{Sr}_2\text{MnTiO}_6$ ceramic in the X-band (at 9.4 GHz) were carried out using the ER 200 SRC Bruker (EMX/plus) and Varian E – 12 spectrometers in temperature ranges 5–320 and 300–680 K, respectively.

XPS analysis was performed in a UHV chamber (base pressure $\sim 5 \times 10^{-10}$ mbar) equipped with Mg K_α X-ray source operating at 12.5 kV and 250 W and Phoibos 150 hemispherical energy analyzer (all from SPECS GmbH, Berlin, Germany). For

high-resolution measurements, we set the pass energy equal to 20 eV (step size of 0.1 eV, 20 scans). Peak shifts due to any apparent changes were calibrated with the adventitious carbon C1s peak set to 284.8 eV. XPS spectra registered from experimental samples were analyzed with the CasaXPS software [26]. The elemental concentrations were retrieved from the area of the detected peaks for each element using sensitivity factors provided by the manufacturer. The phase analysis of the reaction products was performed using crystallographic database “Database of Powder Standard–PDF2” (ICDD, USA, Release 2009 [26–28]). The sample is single-phase one, there are no impurity reflexes. X-ray examination was carried out using the Shimadzu XRD-7000 S automatic diffractometer with exposure 3–5 s in point. X-ray pattern processing was performed with FULLPROF-2018 program.

The microstructure and elemental composition of $\text{Sr}_2\text{MnTiO}_6$ ceramic were studied via scanning electron microscopy (SEM, EVO 50 XVP) and energy-dispersive X-ray spectrometry (EDS, Oxford, Inca Energy 350). The spectrometer was placed inside a SEM.

Magnetization and specific heat measurements were performed on the PPMS-9 device in the temperature range from 4.2 to 300 K in zero-field-cooled (ZFC) and field-cooled (FC) regimes. The magnetic hysteresis loops were measured in the field range up to 9 T.

3 Structural and Microstructural Properties

Theoretical, experimental, and difference diffraction patterns of $\text{Sr}_2\text{MnTiO}_6$ processed by the Rietveld method are presented in Fig. 1. The X-ray diffractions patterns of sample obtained contains no reflections of impurity phases, solid solutions crystallize in the space group Pm3m (No 221), Miller indices (hkl)

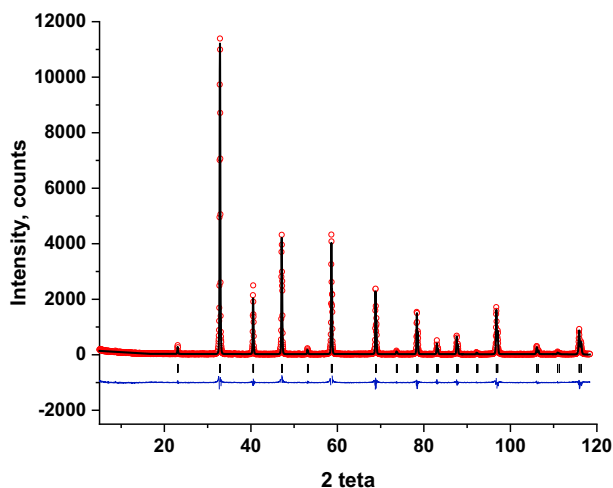


Fig. 1 Theoretical (black line), experimental (red circles) and difference (blue line) diffractograms of $\text{Sr}_2\text{MnTiO}_{5.87}$

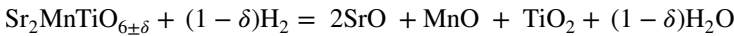
Table 1 Crystallographic data obtained from Rietveld refinements

Atom	Site	x	y	z	B_{iso} (\AA^2)	Occupancy
Sr	1b	0.5	0.5	0.5	0.98(9)	1
Mn	1a	0	0	0	0.54(3)	0.5
Ti	1a	0	0	0	0.54(3)	0.5
O1	3d	0.5	0	0	1.79(8)	2.95(4)
Selected bond lengths (\AA)						
Ti/Mn—O 1.928 (1) \times 6						
Sr—O 2.726 (1) \times 12						
Lattice constants: $a = 3.85542$ (2) \AA						
R-factors $R_{\text{wp}} = 4.53\%$, $R_{\text{exp}} = 4.54\%$, $R_{\text{B}} = 2.58$, $R_{\text{I}} = 2.25$ and $\chi^2 = 2.61$						

correspond to the main phase reflections of the cubic perovskite structure. The obtained crystal chemical parameters of the oxide are presented in Table 1.

The obtained parameter of the cubic lattice $a = 3.85542$ (2) \AA differs somewhat from the value $a = 3.8618$ (1) \AA given in [6], in which it is shown that the experimental diffractogram of $\text{Sr}_2\text{MnTiO}_6$ can be described both on the basis of the cubic cell Pm3m, where Mn^{4+} and Ti^{4+} ions are located in the octahedral environment of oxygen ions. The differences in the values of the parameter a of the cubic unit cell of our sample and the reference data can be attributed to possible oxygen nonstoichiometry of the sample due to non-similar conditions of synthesis and heat treatment. The oxygen content in the sample was determined via the thermogravimetric analysis by reducing hydrogen in the current for 6 h at a temperature of 950 $^\circ\text{C}$.

The $\text{Sr}_2\text{MnTiO}_{6\pm\delta}$ decomposition reaction can be written as.



and the difference in the masses of the initial and final sample attachments can only be correlated to the amount of oxygen released during the reduction. According to the calculation data, the formula of the synthesized oxide corresponds to $\text{Sr}_2\text{MnTiO}_{5.87}$.

Figure 2a shows SEM images of samples ceramic powder $\text{Sr}_2\text{MnTiO}_{5.87}$ obtained using a back-scattered electron detector (QBSD). It can be seen that the $\text{Sr}_2\text{MnTiO}_{5.87}$ sample is a finely dispersed powder with a microparticle size from ≈ 500 nm to ≈ 100 μm . As can be seen from Fig. 2b, microparticles larger than ≈ 10 μm exhibit pores whose size ranges from ≈ 700 nm to ≈ 3 μm .

The elemental composition and its distribution in $\text{Sr}_2\text{MnTiO}_{5.87}$ was studied using energy-dispersive X-ray spectroscopy (EDS). Table 2 presents EDS spectra data from EDS spectrum 2 of the sample. From the EDS spectrum 1, obtained from an area of $\approx 1 \times 1$ mm, it can be seen that the elemental composition corresponds to the units of the formula of the chemical compound $\text{Sr}_2\text{MnTiO}_6$. The increased carbon content was caused by the sample preparation technique, since the fixation of the ceramic powder was carried out using conductive carbon tape. EDS spectra 2 and 4 show that the elemental composition is in good agreement

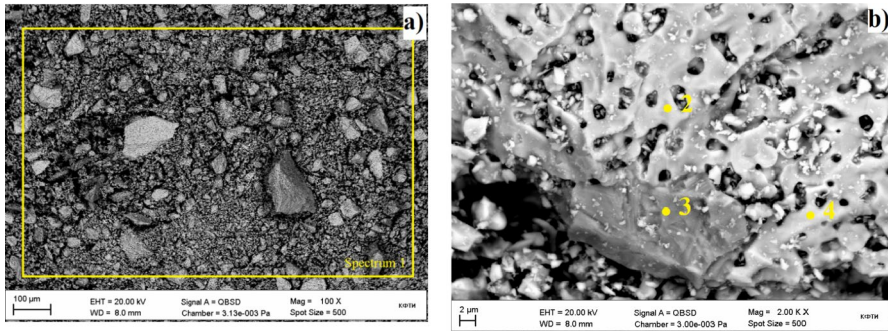


Fig. 2 The SEM images of the $\text{Sr}_2\text{MnTiO}_{5.87}$ ceramic with magnification: **a** 100 X and **b** 2000 X

Table 2 The elemental composition of the $\text{Sr}_2\text{MnTiO}_{5.87}$ ceramic powder obtained by EDS-microanalysis

Spectrum number from a point/square	Contents of chemical elements (at. %)*				
	C	O	Ti	Mn	Sr
2 (point)	5.51	59.26	9.12	9.06	17.05

*Root mean square ≈ 2 at. %

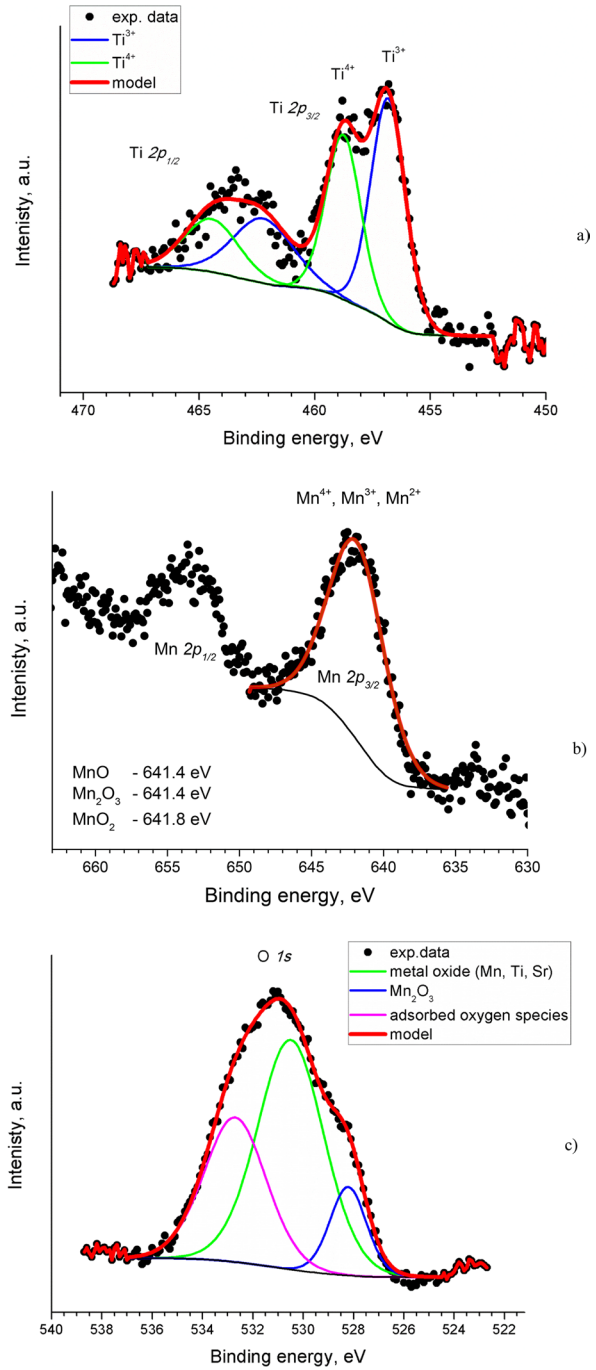
with the compound formula $\text{Sr}_2\text{MnTiO}_6$ and the overall spectrum (Spectrum 1). The carbon content is due to surface contamination. The dead time during the accumulation of EDS spectra was about 15–20%, which corresponds to the detection of the main flux of characteristic X-ray radiation when the sample surface is perpendicular to the electron beam.

The data of EDS spectrum 3 are in agreement with the phase contrast in Fig. 2b, where a low content of heavy elements of the matrix is observed, with the exception of Mn (32.4 at. %).

High-resolution XPS core-level spectra of Ti 2*p*, Mn 2*p*, and O 1*s* energy regions are presented in Fig. 3. As follows from the XPS data, the Ti 2*p*_{3/2} (Fig. 3a) peak can be deconvoluted into two components, namely, the first peak centered at 456.8 eV and the second peak centered at 458.8 eV. These peaks correspond to Ti^{4+} and Ti^{3+} , respectively [28, 29]. The Mn 2*p*_{3/2} main peak is located at 641.8 eV (Fig. 3b) and can be attributed to the Mn oxide ($E_B = 641.4\text{--}641.8$ eV). Determination of the manganese valence is more difficult due to similar binding energy values for Mn_2O_3 or MnO_2 . In order to establish the formation of manganese oxide phases, the deconvolution of the O 1*s* peak was performed.

The O 1*s* XPS spectrum can be fitted by a minimum of three components. Additional experiments were performed using delicate ion beam etching of the surface of sample in order to identify the nature of these components. Two steps of Ar^+ ions etching with an energy of 1000 eV and durations of 30 (see Fig. 3c) and 60 s, respectively, were carried out. The spectra for all three cases can be well described by the sum of three components with peak positions of 528.2 eV, 530.5 eV and 532.7 eV.

Fig. 3 (Color online) XPS spectra observed from $\text{Sr}_2\text{MnTiO}_{5.87}$ ceramics. **a** Ti 2p; **b** Mn 2p; **c** O 1s after the 1st step of Ar^+ ions etching (see text)



At the same time, at steps 1 and 2 of etching, the contribution to the total intensity from the high-energy component decreased by 10 and 7%, respectively. The contributions of the other two components (sub-peaks with medium and low binding energies) at the first step increased comparably, and at the second step, the contribution of the low-energy component increased, while the contribution of the medium-energy component remained unchanged. It should be noticed that the contribution of the component at 530.5 eV dominated and amounted to 45–52% of the integral intensity. In our opinion, these observations allow to unambiguously attribute the high-energy component to all kinds of oxygen-containing adsorbates and the other two components—to the oxygen in the host material [30–32]. It should be pointed out that the fraction of the low-energy XPS component of the sum of the low- and the medium-energy ones after the first step of etching remained at the level of ~20%, and after the second etching step it increased to 31%. This fact, from our point of view, indicates the possible reduction of some manganese ions to the Mn^{3+} [32] state at the second stage of etching and the corresponding increase of the low-energy XPS component intensity. Thus, the 528.2eV component is attributed to Mn^{3+} ions, and an observation of this component in the spectrum of the initial sample indicates the presence of the Mn^{3+} ions in $\text{Sr}_2\text{MnTiO}_{5.87}$ ceramics already after the synthesis.

4 ESR Results

ESR spectra of the $\text{Sr}_2\text{MnTiO}_{5.87}$ ceramic were measured in the temperature range 4.5–320 K using Bruker EMX plus spectrometer. Early, the ESR spectra and fitting results are presented [33] in temperature interval from 300 to 40 K. Here we presented the ESR spectra in the 5–50 K intervals that are shown in Fig. 4a. The fourth ESR lines were used for description ESR spectra.

These ESR spectra can be satisfactorily described by the Lorentzian profile determined by the resonance-field value B_{res} , the linewidth ΔB , and the asymmetry parameter α , where the resonance at inverted field direction is included because of the large line width [35]:

$$\frac{dP}{dB} \propto \frac{d}{dB} \left[\frac{\Delta B + \alpha(B - B_{\text{res}})}{(B - B_{\text{res}})^2 + \Delta B^2} + \frac{\Delta B - \alpha(B + B_{\text{res}})}{(B + B_{\text{res}})^2 + \Delta B^2} \right]. \quad (1)$$

The approximation of magnetic resonance lines using (1) gives the temperature dependencies of the ESR linewidth, the asymmetry parameter α which is near zero, the resonance field B_{res} , and the integral signal intensity (see Fig. 5). One ESR line with the resonance magnetic field in the range of 3400 Oe has a large linewidth above 7000 at low temperatures, and we associated with region where the spin-glass phase from manganese and titanium ions was observed. We do not give temperature dependences of the linewidth and integral intensity of this line in Fig. 5, since the accuracy of determining parameters and trends is small. This ESR line broadening upon approaching $T_{\text{VF}} = 54(2)\text{K}$ may be alternatively described in terms of a Vogel-Fulcher type scenario [37] as shown in [33]. The effects related to formation

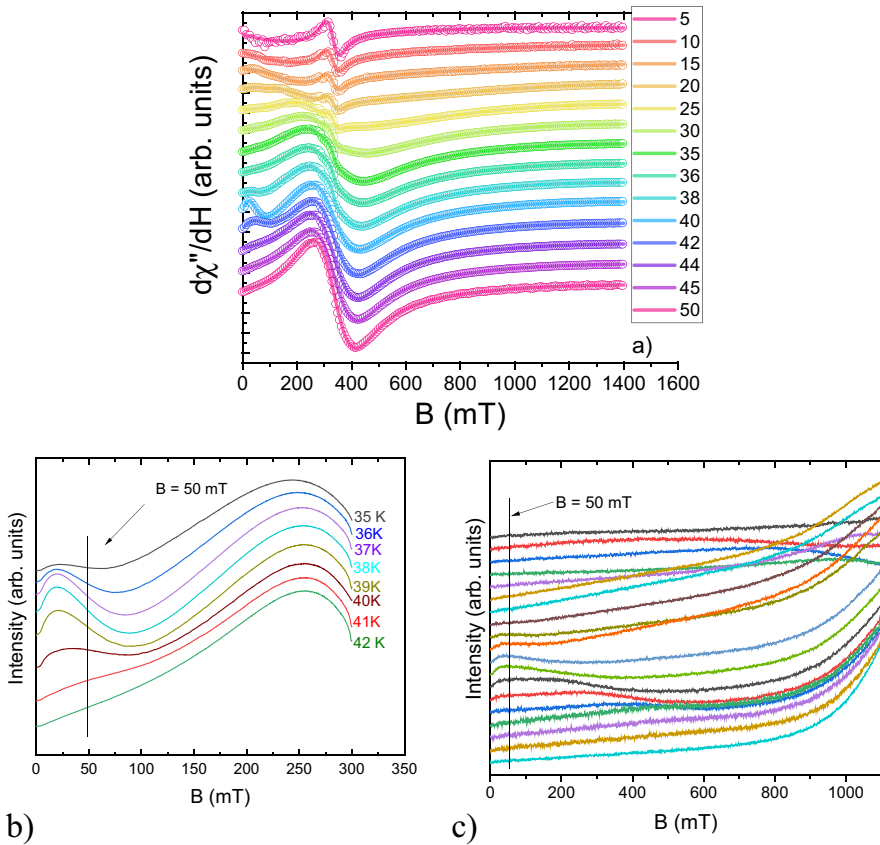


Fig. 4 ESR spectra in $\text{Sr}_2\text{MnTiO}_{5.87}$ as a function of the magnetic field **a** at $T=5\text{--}50$ K; **b** X-band and **c** Q-band at $T=35\text{--}42$ K

of a spin glass are easily observed in ESR experiments sensitive to spin dynamics. Measurements of ESR linewidth show increasing correlations starting at temperatures above the ordered temperature at temperature T_{VF} , which used to describe the spin-freezing process.

The blue triangles in Fig. 5 show the parameters of the ESR line due to the regions formed by manganese ions connected by antiferromagnetic interactions. The linewidth for this ESR line was described as sum two parts where the first term connected with the high-temperature limit of the width of the exchange-narrowed line, which is temperature independent, while the second term is responsible for the critical behavior when approaching the temperature from above, $T_{\text{N}}=37(1)\text{K}$ is the ordering temperature and $\beta=1/3$ is the critical exponent extracted for $\text{Sr}_2\text{MnTiO}_{5.87}$. The value $\beta=1/3$ is typical for 3D antiferromagnets in the Heisenberg model [36].

$$\Delta B = \Delta B_0 + A \cdot \left(\frac{T_{\text{N}}}{T - T_{\text{N}}} \right)^{\beta}. \quad (2)$$

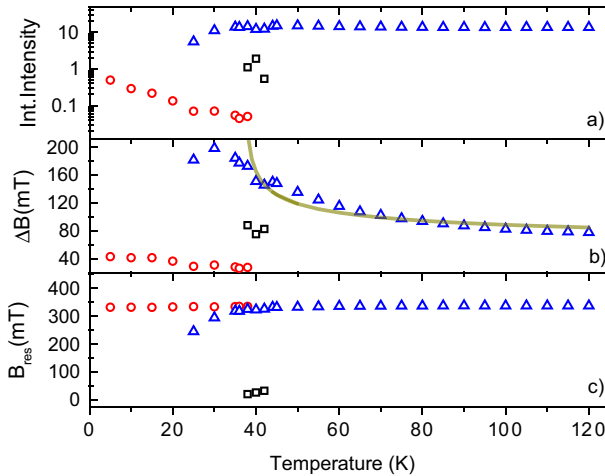


Fig. 5 Temperature dependencies of **a** integral intensity; **b** linewidth; **c** resonance magnetic field of ESR lines in $\text{Sr}_2\text{MnTiO}_{5.87}$

The solid line in Fig. 5 was drawn at the following values: $A=520$ Oe and $\Delta B_0=450$ Oe. These parameters differ somewhat from those given in [33], which is due to a decrease in the synthesis temperature of the second sample. A convincing proof that ESR line is associated with manganese spins connected by antiferromagnetic correlations is the temperature dependence of the integral intensity, which begins to decrease sharply below 37 K.

A narrow ESR line in the sample is convincingly recorded in the magnetic resonance spectrum in the temperature interval from 5 to 40 K. The integral intensity, the linewidth and the resonant magnetic field of this line are shown in Fig. 5 as red circles. This ESR line is associated with the spins of manganese ions at the ends of antiferromagnetic regions and impurity or Ti^{3+} ions.

We believe that the separation of one ESR line into four below the temperature of 100 K connected with the phase separation observed in ceramics $\text{Sr}_2\text{MnTiO}_{5.87}$.

The fourth ESR line with $B_{\text{res}} \approx 50$ mT in X- and Q-bands was observed in small temperature range. Temperature dependencies of the ESR spectra at the X-band frequency of 9.4 GHz and Q-band frequency of 34 GHz for $\text{Sr}_2\text{MnTiO}_{5.87}$ ceramics are shown in Fig. 4b, c at 35–42 K.

The nature of the ESR line is unusual. First of all, it is necessary to note the narrow temperature range of observation of this ESR signal, only a few degrees. Therefore, this line cannot be associated with the presence of an impurity in the sample, the signal from which is usually observed in a wide temperature range. We associate this signal with the formation of correlated regions of spin which form domain walls or skyrmions at $T=37.5\text{--}42.5$ K, in this temperature mode two the phase transitions are registered in the AC magnetization (see Fig. 7) [34].

The analysis of the magnetic resonance spectra indicates phase separation in the sample and the formation of regions with three-dimensional antiferromagnetic ordering at $T_N=37(1)\text{K}$, spin glass at $T_{\text{VF}}=54(2)\text{K}$ and special domains.

The phase transition temperatures are confirmed in the real and imaginary parts of the dynamic susceptibility as will be shown below.

5 Magnetic Properties

Temperature dependencies of magnetization were measured in zero- and nonzero-fields in the range 2–300 K using the PMMS-9 device at Kazan Federal University. The temperature dependences M/H of the inverse magnetization M divided by the magnetic field H at $H=10, 500, 1000,$ and $10,000$ Oe are shown in Fig. 6. The linear part of the inverse magnetic susceptibility above 100 K, approximated by the Curie–Weiss law $X=C/(T-\theta_{CW})$, yields Curie–Weiss temperature $\theta_{CW}=-400$ K. The fact that $\theta_{CW}<0$ indicates the antiferromagnetic nature of isotropic exchange interactions between manganese ions spins in the $\text{Sr}_2\text{MnTiO}_{5.87}$ compound.

Given the Curie parameter $C=2.27$ emu·K/(Oe·mol), the experimental effective magnetic moment $\mu_{\text{eff}} = \sqrt{\frac{3k \cdot C}{N_A}}$ is equal to $\mu_{\text{eff}}=4.27\mu_B$. The assumption that only Mn^{4+} spins with $S=3/2$ contribute to μ_{eff} leads to $\mu_{\text{theor}}=3.87\mu_B$, which is less than the experimental value. In order to explain this discrepancy, we assumed that some manganese and titanium ions of the sample have a valence of 3+: Mn^{3+} ions with $S=2$ and Ti^{3+} ions with $S=1/2$. Since the effective magnetic moment is determined by the expression $\mu_{\text{eff}}^{\text{theory}} = g \cdot (\sum [N_i \cdot S_i(S_i + 1)])^{1/2}$, then taking into account the contributions of manganese ions of different valence Mn^{4+} with $S=3/2$ and Mn^{3+} with spin $S=2$, we estimated the proportion of Mn^{3+} and Mn^{4+} ions as 0.8:0.2, respectively. The second assumption is associated with a change in the valence of a part of titanium ions from 4+ to 3+, also in the respective ratio 0.8:0.2. In this case, we come to $\text{Sr}_2\text{Mn}^{4+}_{0.8}\text{Mn}^{3+}_{0.2}\text{Ti}^{4+}_{0.8}\text{Ti}^{3+}_{0.2}\text{O}^{2-}_{5.87}$ with the effective magnetic moment μ_{theor} being slightly less than the experimental value, $\mu_{\text{eff}}=4.17$. The change in the valence of a part of manganese ions is confirmed by the thermogravimetric analysis.

The static magnetic measurements at $H=10, 500, 1000,$ and $10\,000$ Oe are shown in Fig. 7. We observed three characteristic points in the temperature dependence of magnetization: (i) at 12 K, where ZFC and FC curves experience a peak, (ii) at 39 K, where ZFC curves experience a maximum, and (iii) at 40 K, above which ZFC and FC curves start to coincide at $H=500$ and 1000 Oe. At low external magnetic field values, one can clearly observe a diamagnetic contribution.

Unambiguous determination of the type of magnetic phase transition is only possible by studying the temperature dependence of the alternating-current (AC) magnetization. Temperature dependencies of the real and imaginary parts of the AC magnetization at different frequencies and magnetic-field values in $\text{Sr}_2\text{MnTiO}_{5.87}$ ceramic are shown in Fig. 8. The presence of a peak in the real part of the magnetization at 12 K (Fig. 8c) and its absence in the imaginary indicates (Fig. 8a–b) the transition from an antiferromagnetic to the paramagnetic state in $\text{Sr}_2\text{MnTiO}_{5.87}$ ceramic. The nature of the transition in the temperature range 35–52 K is quite complex. Both real and imaginary parts of the magnetization reach a maximum at 42.5 K (Fig. 8d–f). Another maximum, at 37.5 K (Fig. 8f), is

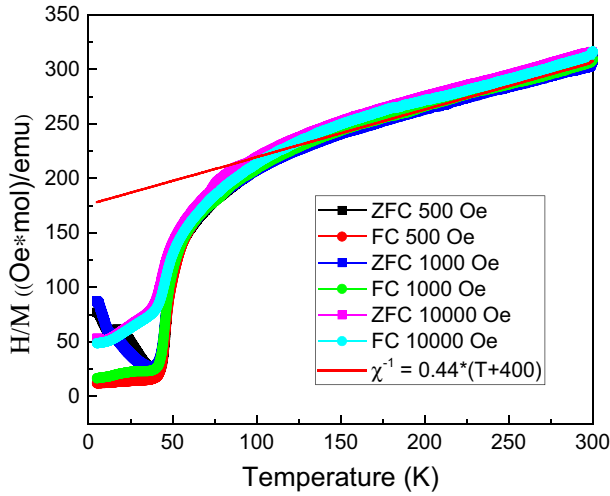


Fig. 6 Inverse magnetization M divided by magnetic field H in $\text{Sr}_2\text{MnTiO}_{5.87}$ as a function of temperature measured in ZFC and FC regimes at $H=0.5$ kOe, 1 kOe, and 10 kOe. The red line shows the Curie-Weiss law

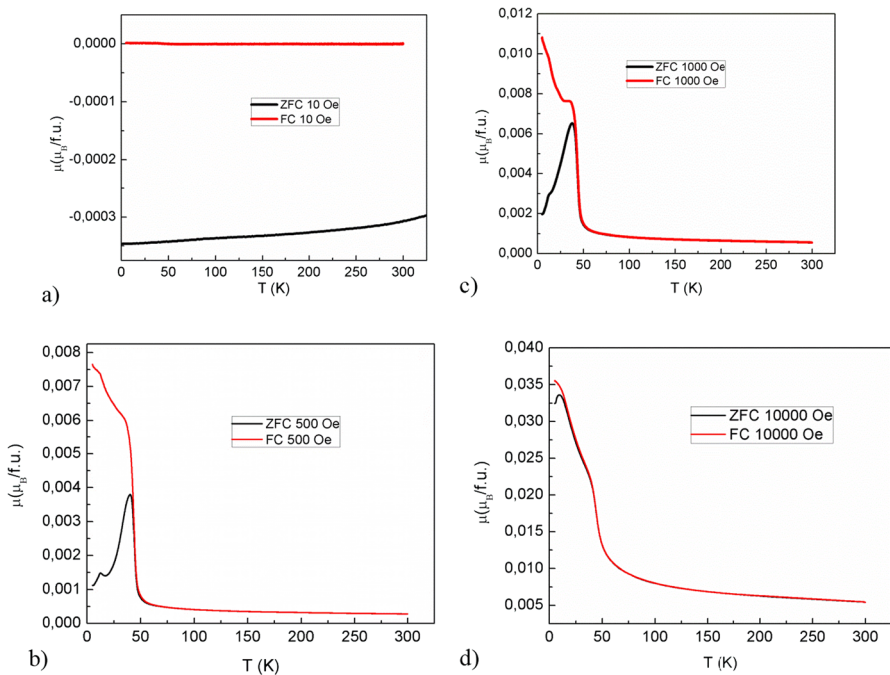


Fig. 7 Static magnetization in $\text{Sr}_2\text{MnTiO}_{5.87}$ as a function of temperature measured in ZFC and FC regimes in the external magnetic field with $H = \mathbf{a}$ 10, **b** 500 Oe, **c** 1000 Oe, and **d** 10,000 Oe

observed only in the real part of the magnetization. At 45–50 K, real and imaginary parts feature a plateau and then, at ~52 K, start to decrease with temperature. Also, both real and imaginary parts of the magnetization increase with the increasing magnetic field.

Magnetic field dependencies of the magnetization in $\text{Sr}_2\text{MnTiO}_{5.87}$ compound at different temperatures are shown in Fig. 9. Obtained at $T=5, 15,$ and 25 K, these curves can be adequately fitted by a sum of two terms:

$$M(H) = M_{\text{ferro}} + \chi H \quad (3)$$

The first terms can be written as $M_{\text{ferro}} = (2M_S/\pi) \cdot \tan^{-1}[(H \pm H_C)/H_T]$, where M_S is the saturation magnetization, H_T is the inner local field of uniaxial anisotropy, and H_C is the coercive field. The second term χH is the magnetic contribution from the paramagnetic part [38]. The fitting parameters in Eq. (3) are given in Table 3. While only one ferrimagnetic contribution is needed to describe the behavior of magnetization at 5, 15, 25, 45 K, at 40 and 45 K the second contribution is needed for a correct fitting. This insight suggests phase separation at 40 and 45 K.

6 Specific Heat

The specific heat was measured by the relaxation method using a Physical Property Measurement System (PPMS) (Quantum Design) in the temperature range 4–300 K and in a magnetic field up to 9 T. Figure 10 shows the specific heat $C(T)/T$ as a function of temperature for $\text{Sr}_2\text{MnTiO}_{5.87}$ ceramic measured in zero, 3 T, 6 T, and 9 T magnetic fields. The lambda point in the temperature dependence of the heat capacity is not observed indicating the absence of structural changes. We approximate the temperature dependences of the specific heat capacity using the equation

$$C = C_{\text{latt}} + C_{\text{M}} + \gamma \cdot T, \quad (4)$$

where C_{latt} , C_{M} , and $\gamma \cdot T$ correspond to the lattice, the magnetic, and the linear contributions, respectively. To extract the magnetic contribution, we approximate C_{latt} and $\gamma \cdot T$ according to the standard procedure. The lattice contribution C_{latt} is approximated using a sum of one isotropic Debye (C_{D}) term accounting for 3 acoustic phonon branches and three isotropic Einstein terms (C_{E1} , C_{E2} , C_{E3}) averaging the $3s-3=27$ optical phonon branches [38]:

$$C_{\text{latt}} = a_{\text{D}} \cdot C_{\text{D}} + a_{\text{E1}} \cdot C_{\text{E1}} + a_{\text{E2}} \cdot C_{\text{E2}} + a_{\text{E3}} \cdot C_{\text{E3}}. \quad (5)$$

The best fit of the experimental data was obtained with the ratio between terms in Eq. (5) being fixed as $\alpha_{\text{D}}:\alpha_{\text{E1}}:\alpha_{\text{E2}}:\alpha_{\text{E3}}=1:3:3:3$.

Debye's contribution to the specific heat capacity can be calculated as:

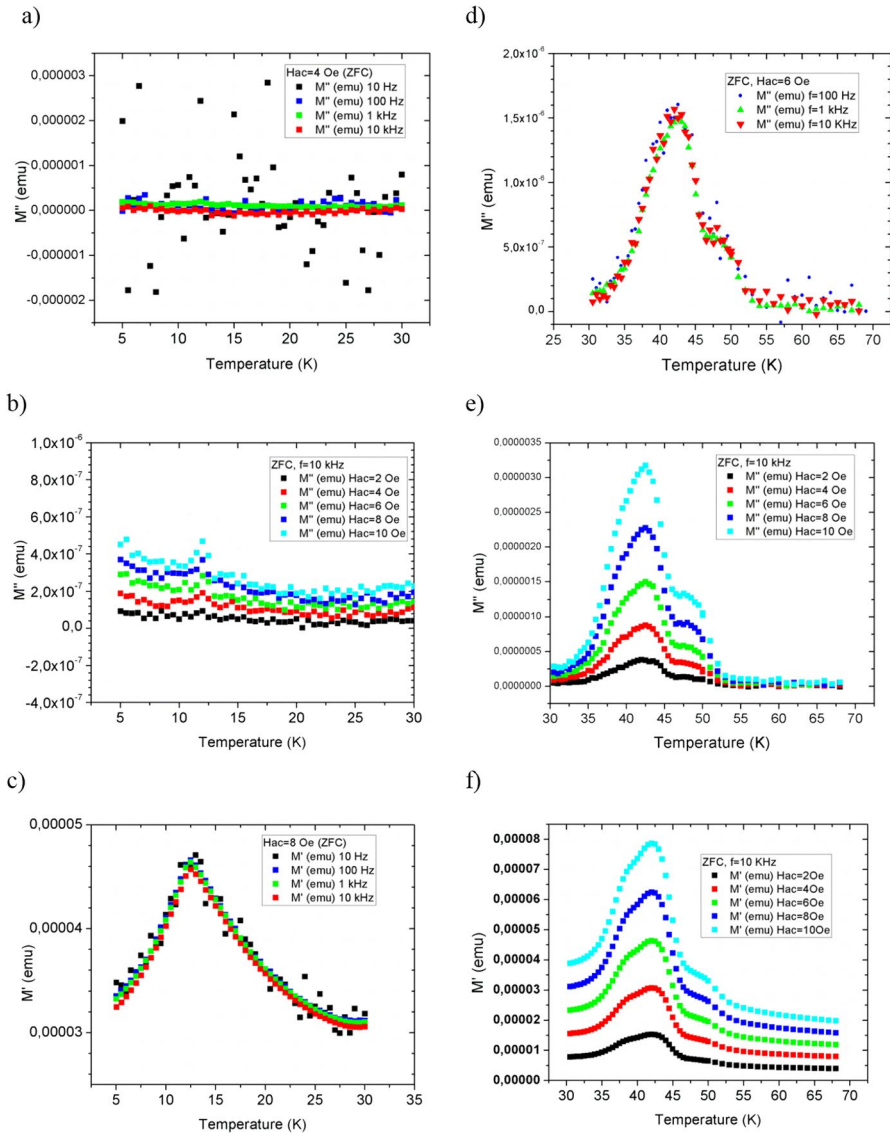


Fig. 8 Real and imaginary parts of the AC magnetization in $\text{Sr}_2\text{MnTiO}_{5.87}$ ceramics as a function of temperature at different frequencies and magnetic-field values in the temperature ranges **a–b** imaginary and **c** real parts and in **30–67 K d–e** imaginary and **f** real parts

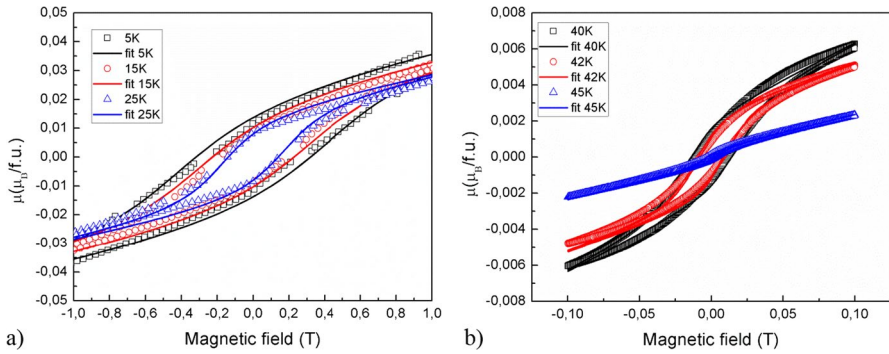


Fig. 9 Hysteresis loops of Sr₂MnTiO_{5.87} ceramic at **a** 5, 15, 25 K and **b** 40, 42, 45 K

Table 3 Magnetic hysteresis loop characteristics of Sr₂MnTiO_{5.87} compound at different temperatures. *M_S* and *χ* are given in *μ_B/f.u./Oe*, *H_C* and *H_T* are given in Oe

T (K)	<i>M_{S1}</i> (<i>μ_B</i>)	<i>H_{C1}</i> (Oe)	<i>H_{T1}</i> (Oe)	<i>M_{S2}</i> (<i>μ_B</i>)	<i>H_{C2}</i> (Oe)	<i>H_{T2}</i> (Oe)	<i>aχ</i> (<i>μ_B/Oe</i>)
5	0.0287	4000	4500	–	–	–	1.25*10 ⁻⁶
15	0.0250	3000	4000	–	–	–	1.25*10 ⁻⁶
25	0.0179	1700	2000	–	–	–	1.25*10 ⁻⁶
40	0.0009	75	100	0.0018	275	130	4.14*10 ⁻⁶
42	0.001	40	120	0.0018	155	150	2.6*10 ⁻⁶
45	0.00041	50	70	–	–	–	1.98*10 ⁻⁶

$$C_D = 9R \left(\frac{T}{\theta_D} \right)^3 \int_0^{\theta_D/T} \frac{x^4 e^x}{(e^x - 1)^2} dx. \tag{6}$$

Einstein’s contribution to the specific heat is given by the equation:

$$C_E = 3R \left(\frac{\hbar\omega}{kT} \right)^2 \frac{\exp\left(\frac{\hbar\omega}{kT}\right)}{\left(\exp\left(\frac{\hbar\omega}{kT}\right) - 1\right)^2}. \tag{7}$$

The Einstein temperatures were calculated using the ratio $\hbar\omega = k\theta_E$. Debye and Einstein temperatures are equal to $\theta_D=217$ K, $\theta_{E1}=275$ K, $\theta_{E2}=615$ K, $\theta_{E3}=2000$ K from fitting procedure. The calculated lattice contribution agrees with the experimental data very well (black line in Fig. 10). The magnetic contribution to the lattice heat capacity, obtained after subtracting the lattice and linear parts, is shown in the inset of Fig. 10. The linear-term coefficient of the specific heat is $\gamma=0.02$ J/K. This procedure allowed to reveal anomalies in $C_M(T)/T$ at $T_N=10.1$ K

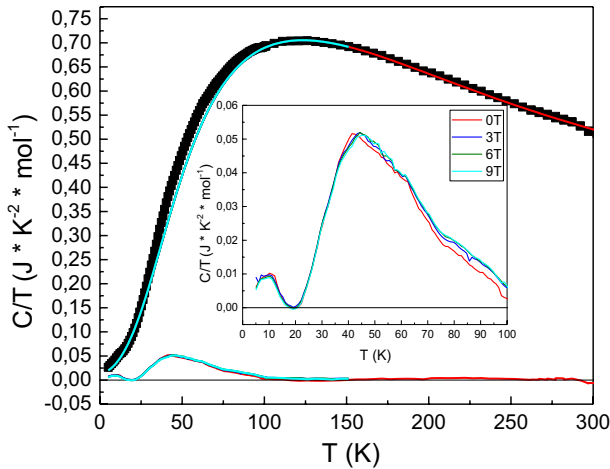


Fig. 10 Specific heat $C(T)/T$ of $\text{Sr}_2\text{MnTiO}_{5.87}$ as a function of temperature measured at $H=0, 3, 6,$ and 9 T. The inset shows the magnetic part of the specific heat in the temperature range $4\text{--}90$ K after subtracting the calculated lattice and linear contributions; the black solid line is the fitting curve (see details in the text)

and $T_C=41.3$ K (Fig. 11 and inset in Fig. 10). These temperatures coincide with the temperatures at which anomalies in the $M(T)$ dependence were observed previously.

7 Discussion

The double perovskites and ordinary perovskites differ in the degree of disorder in the arrangement of the two types of ions in position B. Structural and X-ray photoelectron spectroscopic studies have been performed on bulk pellet sample of the ordinary perovskite with substitute ions $\text{SrTi}_{0.5}\text{Mn}_{0.5}\text{O}_3$ to confirm the antisite disorder and charge state of different ions (Ti, O and Mn). The XPS spectra of titanium (Ti) 2p, oxygen (O) 1s and manganese (Mn) 2p core levels have been performed to confirm the multiple charge states of individual ions present in the sample prepared via solid-state reaction route [39]. The observation of phase transitions near 40 K in the studied samples and their absence in the $\text{SrTi}_{0.5}\text{Mn}_{0.5}\text{O}_3$ samples indicates an ordering in the distribution of manganese and titanium ions.

The appearance of an additional ESR line between 37.5 and 42.5 K with $B_{\text{res}}=50$ mT in the magnetic resonance spectrum requires careful consideration. First of all, it should be noted that the typical g-factor of manganese and titanium ions in dielectric matrix differ slightly from 2 [40]. Since the resonance magnetic field ESR signal is shifted to the region of low magnetic fields, the resonance condition takes the form: $h\nu = g\mu_B(B + B_{\text{intra}})$. In the presence of an internal local field, the resonance condition for the magnetic resonance $h\nu = g_{\text{eff}}\mu_B B_{\text{res}}$ is fulfilled at a lower value of the external magnetic field. However, the resonant value of the magnetic field in the X- and Q-bands practically was coincided $B_{\text{res}}\approx 50\text{mT}$, which indicates the antiferromagnetic nature of the observed signal but not ferromagnetic.

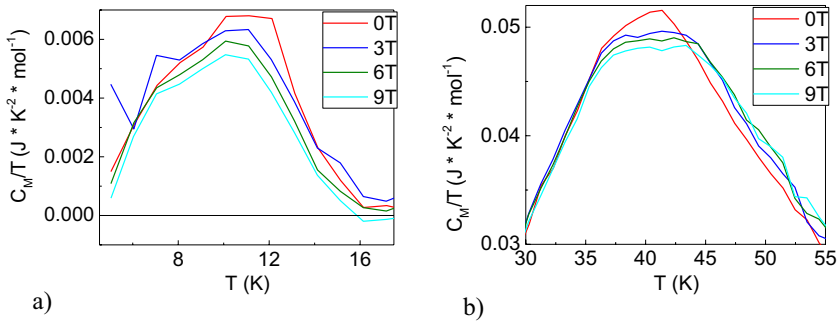


Fig. 11 Specific heat $C(T)/T$ of $\text{Sr}_2\text{MnTiO}_{5.87}$ ceramics as a function of temperature measured at $H=0, 3, 6, 9$ T and $T=\mathbf{a}$ 4–16 K and \mathbf{b} 37–48 K

It should be noted that this ESR line does not change the value of the resonance field while the temperature changes, the ESR line with $B_{\text{res}}=50$ mT appears at 37.5 K and is observed up to 42.5 K, and then disappears. Such narrow temperature range for existence of the micro-regions was previously observed in MnSi [41] with temperatures from 27 to 30 K in magnetic fields from ~ 0.1 to 0.22 T, which the authors associate with the formation of skyrmions. Typical variations of skyrmions are Bloch-type ($Q=-1$), Néel-type ($Q=-1$), antiskyrmion ($Q=+1$), biskyrmion with $Q=-2$, antimeron with $Q=+1/2$, meron with $Q=-1/2$, hedgehog with $Q=+1$, antihedgehog with $Q=-1$ and were described in the review [42]. Probably, the micro-regions with a vortex character of the spins arrangement are formed in $\text{Sr}_2\text{MnTiO}_{5.87}$ ceramics, which is confirmed by small value of the effective magnetic moment (see Fig. 9). The dimensions of the skyrmion regions, according to [42], can be several nm or about 30 lattice periods.

The observation ESR lines in the magnetic resonance spectrum indicates the presence of two phases in the sample with different magnetic properties, which is confirmed by the presence of two ferromagnetic contributions necessary to describe hysteresis loops in the temperature range from 39 to 42 K, see Table 3, with different values the saturation magnetization, the inner local field of uniaxial anisotropy, and the coercive force. In the temperature dependence of the real part of the magnetization measured at alternating current, two peaks are also observed at $T=37$ K and $T=42$ K (Fig. 8f), which is consistent with the behavior of the magnetic contribution to the specific heat (Fig. 11b).

The second possible reason for observing the fourth EPR line is the transition on the Yafet-Kittel phase. The temperature range between the Yafet-Kittel phase at $T_N=42$ K and the incommensurate phase at $T_1=40$ K in Mn_3O_4 coincides with the temperature range where the fourth ESR line is observed [43]. It is reasonable to assume that the fourth ESR line is associated with antiferromagnetic resonance. However, in the temperature dependence of the Mn_3O_4 ESR spectra, the presence of an additional line with a very large g -factor was not reported. Probably, the resonant magnetic field for the ESR line with resonance magnetic field about 50 mT linked to the magnetic field of the spin flop transition in MnO_6 chain formed in $\text{Sr}_2\text{MnTiO}_{5.87}$.

A complex phase pattern of magnetic transitions for an antiferromagnetic MnO_6 chain in an octahedron was predicted in [43].

We assume that the skyrmion structure or antiferromagnetic domain walls were formed in the temperature range 37.5–42.5 K. That is indirectly confirmed by presence of diamagnetic contribution at low external magnetic field 10 Oe.

8 Conclusion

The synthesis of $\text{Sr}_2\text{MnTiO}_{5.87}$ ceramics was carried out by the solution combustion precursor method. The oxygen content, estimated by the thermogravimetric method, is equal to 5.87. Due to the oxygen deficiency of transition metal ions, titanium and manganese have a variable valence of Ti^{3+} , Ti^{4+} , Mn^{3+} , and Mn^{4+} which is confirmed by XPS and analysis of the high-temperature part of the magnetic susceptibility. The joint thermogravimetric and effective-magnetic-moment analysis of the experimental data allowed to estimate the ratio between three and four-valent manganese and titanium elements as $N_{\text{Ti}}(\text{Ti}^{3+}:\text{Ti}^{4+}) = N_{\text{Mn}}(\text{Mn}^{3+}:\text{Mn}^{4+}) = 0.2:0.8$. We observed peaks in the experimental curves of real and imaginary parts of AC magnetization and the ESR line with $B_{\text{res}} \approx 50\text{mT}$ in spectra in the temperature range 37.5–42.5 K. The analysis of the measured temperature dependence of the specific heat capacity made it possible to estimate the Debye and Einstein temperatures, as well as to obtain magnetic contributions to the heat capacity by subtracting the lattice contribution from experimental data. The maxima of the magnetic specific heat contribution are observed at temperatures of 12 K and 42.5 K, which are consistent with the temperatures of phase transitions in the temperature dependence of magnetization to Yafet-Kittel phase at $T_N = 42.5$ K and into a canted antiferromagnetic phase at $T_N = 12$ K. In addition, this compound shows another transition at $T_{\text{IPh}} \approx 37.5$ K, to an incommensurate phase.

Acknowledgements This research was supported by the Russian Science Foundation (Project No. 22-42-02014) and DST Project number DST/INT/RUS/RSF/P-55/2021.

Author contribution DVP—acquired data visualization, writing an article (review and editing). IVY—ESR measurement in X-band. RGB—magnetization measurements. MAC—specific heat data measurements. IRV—XPS measurements. RVY—interpretation of XPS. IAF—SEM experiment. TIC—fit of X-ray data and synthesis of the sample. YAD—synthesis of the sample. IIF—ESR measurement in Q-band. TM—conceptualization, writing an article (review and editing). RME—writing an article (original draft), supervision.

Funding This research was supported by the Russian Science Foundation (Project No. 22-42-02014) and DST Project number DST/INT/RUS/RSF/P-55/2021.

Availability of data and materials Data and materials are available on request.

Declarations

Conflict of interest No competing interest.

Ethical approval Not applicable.

References

1. M.D.C. Viola, M. Martinez-Lope, J. Alonso, P. Velasco, J. Martinez, J. Pedragosa, R. Carbonio, V. Fernandes-Diaz, *Chem. Mater.* **14**, 812–818 (2002). <https://doi.org/10.1021/cm011186j>
2. K.-I. Kobayashi, T. Kimura, H. Sawada, K. Terakura, Y. Tokura, *Nature* **395**, 677–680 (1998). <https://doi.org/10.1038/27167>
3. Y. Lin, X. Chen, X. Liu, *Solid State Commun.* **149**, 784–787 (2009). <https://doi.org/10.1016/j.ssc.2009.02.028>
4. O.N. Meetei, O. Erten, A. Mukherjee, M. Randeria, N. Trivedi, P. Woodward, *Phys. Rev. B* **87**, 165104 (2013). <https://doi.org/10.1103/PhysRevB.87.165104>
5. O. Erten, O.N. Meetei, A. Mukherjee, M. Randeria, N. Trivedi, P. Woodward, *Phys. Rev. B* **87**, 165105 (2013). <https://doi.org/10.1103/PhysRevB.87.165105>
6. T. Saha-Dasgupta, J. Supercond. and Novel Magn. **26**, 1991–1995 (2013). <https://doi.org/10.1007/s10948-012-1920-7>
7. C. Ritter, M. Ibarra, L. Morellon, J. Blasco, J. Garcia, J. Teresa, J. Phys. Condens. Matter **12**, 8295–8308 (2000). <https://doi.org/10.1088/0953-8984/12/38/306>
8. M. Sanjuan, M. Laguna, *Phys. Rev. B* **64**, 174305 (2001). <https://doi.org/10.1103/PhysRevB.64.174305>
9. M. Retuerto, M. Garcia-Hernandez, M. Martinez-Lope, M. Fernandez-Diaz, J. Atfield, J. Alonso, J. Mater. Chem. **17**, 3555–3561 (2007). <https://doi.org/10.1039/B705797K>
10. D. Serrate, J. De Teresa, M. Idarra, J. Phys. Condens. Matter **19**, 023201 (2006). <https://doi.org/10.1088/0953-8984/19/2/023201>
11. J.-W.G. Bos, J.P. Atfield, *Phys. Rev. B* **70**, 174434 (2004). <https://doi.org/10.1103/PhysRevB.70.174434>
12. S. Kumar, G. Giovannetti, J. van den Brink, S. Picozzi, *Phys. Rev. B* **82**, 134429 (2010). <https://doi.org/10.1103/PhysRevB.82.134429>
13. P.N. Lekshmi, S.S. Pillai, K.G. Suresh, P.N. Santhosh, M.R. Varma, J. Alloys Compd. **522**, 90–95 (2012). <https://doi.org/10.1016/j.jallcom.2012.01.091>
14. O. Mustonen, S. Vasala, E. Sadrollahi, K.P. Schmidt, C. Baines, H.C. Walker, I. Terasaki, F.J. Litterst, E. Baggio-Saitovitch, M. Karppinen, *Nat. Commun.* **9**, 1085 (2018). <https://doi.org/10.1038/s41467-018-03435-1>
15. R. Mizaras, A. Loidl, *Phys. Rev. B* **56**, 726–729 (1997). <https://doi.org/10.1103/PhysRevB.56.10726>
16. P. Aich, C. Meneghini, L. Tortora, V. Siruguri, S.D. Kaushik, D. Fuf, S. Ray, J. Mater. Chem. C **7**, 3560 (2019). <https://doi.org/10.1039/C8TC04293D>
17. U. Bhardwaj, A. Sharma, A. Mathur, A. Halder, H.S. Kushwaha, *Energy Storage* **4**, 293 (2022). <https://doi.org/10.1002/est2.293>
18. A. Sharma, U. Bhardwaj, H.S. Kushwaha, *Clean. Eng. Technol.* **2**, 100087 (2021). <https://doi.org/10.1016/j.clet.2021.100087>
19. J. Roa-Rojas, C. Salazar M, D. Llamasa P, A.A. León-Vanegas, D.L. Téllez, P. Pureur, F.T. Dias, V.N. Vieira, J. Magn. Mater. **320**, 104–e106 (2008). <https://doi.org/10.1016/j.jmmm.2008.02.023>
20. D. Landinez-Tellez, G. Pena-Rodriguez, F. Fajardo, J. Arbey Rodriguez M, J. Roa-Rojas, *Dyna* **79**(171), 111–115 (2012)
21. J. Lamsal, R. Mondal, A. Kumar, K. Kamala Bharathi, P.N. Santhosh, R. Nirmala, A.K. Nigam, W.B. Yelon, S. Quezado, S.K. Malik, J. Appl. Phys. **109**, 07E329 (2011). <https://doi.org/10.1063/1.3562917>
22. S. Sharma, K. Singh, R. Rawat, N.P. Lalla, J. Alloys Compd. **693**, 188–193 (2017). <https://doi.org/10.1016/j.jallcom.2016.09.179>
23. I. Qasim, B.J. Kennedy, J. Solid State Chem. **200**, 39–42 (2013). <https://doi.org/10.1016/j.jssc.2013.01.011>
24. S. Sharma, P. Yadav, T. Sau, P. Yanda, P.J. Baker, I. da Silva, A. Sundaresan, N.P. Lalla, J. Magn. Mater. **492**, 165671 (2019). <https://doi.org/10.1016/j.jmmm.2019.165671>
25. K.P. Meher, M. Savinov, S. Kamba, V. Goian, K.B.R. Varma, J. Appl. Phys. **108**, 094108 (2010). <https://doi.org/10.1063/1.3500369>
26. N. Fairley, V. Fernandez, M. Richard-Plouet, C. Guillot-Deudon, J. Walton, E. Smith, D. Flahaut, M. Greiner, M. Biesinger, S. Tougaard, D. Morgan, J. Baltrusaitis, *Appl. Surf. Sci. Adv.* **5**, 100112 (2021). <https://doi.org/10.1016/j.apsadv.2021.100112>

27. J. Lu, L. Si, Q. Zhang, C. Tian, X. Liu, C. Song, J. Zhang, *Adv. Mater.* **33**, 2102525 (2021). <https://doi.org/10.1002/adma.202102525>
28. C.D. Wanger, W.M. Riggs, L.E. Davis, J.F. Moulder, G.E. Muilenberg, *Handbook of X-ray photoelectron spectroscopy: a reference book of standard data for use in X-ray photoelectron spectroscopy* (Perkin-Elmer Corp., Physical Electronics Division, Eden Prairie, 1979)
29. NIST X-ray Photoelectron Spectroscopy Database, *NIST Standard Reference Database Number 20* (National Institute of Standards and Technology, Gaithersburg, 2000), p.20899. <https://doi.org/10.18434/T4T88K> (retrieved 25.08.2022)
30. H. Wu, X.H. Zhu, *J. Am. Ceram. Soc.* **102**, 4698–4709 (2019). <https://doi.org/10.1111/jace.16348>
31. R.Q. Tan, Y.F. Zhu, *Appl. Catal. B-Environ.* **58**, 61–68 (2005). <https://doi.org/10.1016/j.apcatb.2004.12.003>
32. S. Kaliaguine, A. Van Neste, V. Szabo, J.E. Gallot, M. Bassir, R. Muzychuk, *Appl. Catal. A General* **209**, 345–358 (2001). [https://doi.org/10.1016/S0926-860X\(00\)00779-1](https://doi.org/10.1016/S0926-860X(00)00779-1)
33. I.V. Yatsyk, R.M. Eremina, T.I. Chupakhina, Y.A. Deeva, *Magn. Reson. Solids* **24**, 22202 (2022). <https://doi.org/10.26907/mrsej-22202>
34. C. Ross, M. Nitta, *Phys. Rev. B* **107**(2), 024422 (2023). <https://doi.org/10.1103/PhysRevB.107.024422>
35. J.P. Joshi, S.V. Bhat, *J. Magn. Reson.* **168**, 284 (2004). <https://doi.org/10.1016/j.jmr.2004.03.018>
36. T. Vasilchikova, A. Vasiliev, M. Evstigneeva, V. Nalbandyan, J.S. Lee, H.J. Koo, M.H. Whangbo, *Materials*. **15**, 2563 (2022). <https://doi.org/10.3390/ma15072563>
37. M. Balanda, H.K. von Nidda, M. Heinrich, A. Loidl, *Relaxation phenomena liquid crystals, magnetic systems, polymers, high-*T_c* superconductors metallic glasses* (Springer Berlin Heidelberg, Berlin, 2003), pp.89–135. https://doi.org/10.1007/978-3-662-09747-2_3
38. D.V. Popov, T.P. Gavrilova, I.F. Gilmudtinov, M.A. Cherosov, V.A. Shustov, E.M. Moshkina, L.N. Bezmaternykh, R.M. Eremina, *J Phys Chem Solids* **148**(109695), 1–7 (2021). <https://doi.org/10.1016/j.jpcs.2020.109695>
39. S. Sharma, N.P. Lalla, *AIP Conf. Proc.* **1832**, 090010 (2017). <https://doi.org/10.1063/1.4980563>
40. A. Abragam, B. Bleaney, *ESR of Transition Ions* (Clarendon Press, Oxford, 1970)
41. S. Muhlbauer, B. Binz, F. Jonietz, C. Pfleiderer, F. Rosch, A. Neubauer, R. Georgii, P. Boni, *Science* **323**, 915–919 (2009). <https://doi.org/10.1126/science.1166767>
42. Y. Tokura, N. Kanazawa, *Chem. Rev.* **121**, 2857–2897 (2021). <https://doi.org/10.1021/acs.chemrev.0c00297>
43. N.P. Kolmakova, S.A. Kolonogii, M.Y. Nekrasova, R.Z. Levitin, *Phys. Solid State* **41**, 1649–1651 (1999). <https://doi.org/10.1134/1.1131063>

Publisher's Note Springer Nature remains neutral with regard to jurisdictional claims in published maps and institutional affiliations.

Springer Nature or its licensor (e.g. a society or other partner) holds exclusive rights to this article under a publishing agreement with the author(s) or other rightsholder(s); author self-archiving of the accepted manuscript version of this article is solely governed by the terms of such publishing agreement and applicable law.